DOI:10.1190/segam2020-3427411.1

High-resolution source location with sparsity-promoting interferometric cross-correlation migration

Yujin Liu and Yue Du, Aramco Beijing Research Center, Aramco Asia; Yi Luo, EXPEC Advanced Research Center, Saudi Aramco*

Summary

Seismic source localization plays an important role in estimating the hypocenter of earthquakes and in monitoring hydraulic fracturing. Interferometric cross-correlation migration (ICCM) is one of the most important waveform-based source location methods that produces source image from interstation cross-correlations without manual picking. However, the ICCM method suffers from blurring source image, especially for cases when the acquisition aperture is limited, receivers are sparsely distributed and data signal-to-noise is too low. One possible solution is least-squares interferometric cross-correlation migration (LS-ICCM). It fits a source distribution function to the observed interstation cross-correlations by least-squares minimization of misfit, where the source distribution function is source power-spectral density (PSD) defined as a function of frequency and spatial location. To further improve the image resolution, we propose sparsity-promoting interferometric cross-correlation migration (SP-ICCM) method, which impose sparsity constrains on the source PSD in space to mitigate the loss of resolution that arises as a consequence of incomplete information. Through synthetic and field data tests, we demonstrate that our method is robust to noise and effective for close spacing sources.

Introduction

Source locating of passive seismic events is of great importance for determining earthquake hypocenters in seismology (Thurber and Engdahl, 2000) and monitoring hydraulic fractures in exploration geophysics (Maxwell et al., 2010; Shapiro, 2015). Source locations are usually determined by the ray-based methods using picked arrival times and a given velocity model (Pujol, 2004). For example, the double-difference method estimates the source locations by minimizing the residuals between the theoretical and observed travel-time differences for pairs of earthquakes at each station while linking together all observed event-station pairs (Waldhauser and Ellsworth, 2000; Zhang and Thurber, 2003). For these methods, arrival time picking is an inevitable step and has to be performed manually or automatically. Hand picking process is tedious, labor intensive, vulnerable to human biases and time consuming; auto picking may be unreliable for complicated phases or low signal-to-noise ratio (SNR) datasets.

One class of waveform-based source localization method without traveltime picking is interferometric cross-correlation migration (ICCM), which utilizes interstation cross-correlograms to determine the source distribution (Schuster et al., 2004). However, as Schuster et al. (2004) point out, the spatial resolution of the source image is poor mainly due to the reason that the vertical wavenumber of model spectrum provided by the ICCM method is small for limited aperture and sparse sampling acquisition. Similar to the study of solar structure and dynamics in helioseismology, there are numerous investigations in constructing sensitivity kernel of ensemble cross-correlation measurements to variations in seismic source distribution (Basini et al., 2013; Hanasoge, 2013, 2014; Fichtner, 2014; Ermert et al., 2016). However, most of these studies focus on the effects of noise source distribution on ambient noise tomography; little attention has been paid to address the issue related to the lack of spatial resolution in the cross-correlation imaging of seismic sources.

In this abstract, we present a sparsity-promoting cross-correlation waveform inversion method to improve the spatial resolution of the source image. Sparseness in the source distribution function is a valid and useful criterion for supplying the missing information. This is equivalent somehow to assuming smooth amplitude variation in the transition between known and unknown (missing) data. We first review the forward problem that describes how the source power-spectral density (PSD) distribution forward maps to the interstation cross-correlations. Then we introduce both least-squares and sparsity-promoting solution to invert this forward map. Through synthetic and field data experiments, we demonstrate the effectiveness of our proposed sparsity-promotion method for situations of increasing complexity including noise and realistic geology.

Method

We first review the forward problem that simulates interstation cross-correlograms from the source PSD. Then, we present two waveform inversion methods to estimate the source PSD from the observed cross-correlograms: least-squares interferometric cross-correlation migration (LS-ICCM) and sparsity-promoting interferometric cross-correlation migration (SP-ICCM).

Forward problem

Seismic wavefield $u(\boldsymbol{x}_{r_i}, \omega)$ at $\boldsymbol{x}_{r_i}$ is connected with sources at $\boldsymbol{x}_{s_n}$ by the representation theorem (Aki & Richards, 2002)

10.1190/segam2020-3427411.1

$$u(\boldsymbol{x}_{r_i},\omega)=\sum_{n=1}^{N_s} S(\boldsymbol{x}_{s_n},\omega)G(\boldsymbol{x}_{r_i},\boldsymbol{x}_{s_n},\omega)\ , \tag{1}$$

where ω is the angular frequency, N_s is the total number of sources, $S(\boldsymbol{x}_{s_n},\omega)$ is the frequency spectrum of a source at $\boldsymbol{x}_{s_n}$, and $G(\boldsymbol{x}_{r_i},\boldsymbol{x}_{s_n},\omega)$ is the Green's function. The cross-correlation between the seismic wavefield at $\boldsymbol{x}_{r_i}$ and $\boldsymbol{x}_{r_j}$ can be expressed as

$$\begin{aligned}C\left(\boldsymbol{x}_{r_i},\boldsymbol{x}_{r_j},\omega\right) &= u^*(\boldsymbol{x}_{r_i},\omega)u\left(\boldsymbol{x}_{r_j},\omega\right)\\ &=\sum_{m=1}^{N_s}\sum_{n=1}^{N_s} S^*(\boldsymbol{x}_{s_m},\omega)G^*(\boldsymbol{x}_{r_i},\boldsymbol{x}_{s_m},\omega)S(\boldsymbol{x}_{s_n},\omega)G\left(\boldsymbol{x}_{r_j},\boldsymbol{x}_{s_n},\omega\right),\end{aligned} \tag{2}$$

where $u^*(\boldsymbol{x}_{r_i},\omega)$ is the complex conjugate of $u(\boldsymbol{x}_{r_i},\omega)$. Due to the transient nature of seismic sources, $C\left(\boldsymbol{x}_{r_i},\boldsymbol{x}_{r_j},\omega\right)$ is generally different when using different time intervals. We therefore consider the expectation

$$\begin{aligned}E\left[C\left(\boldsymbol{x}_{r_i},\boldsymbol{x}_{r_j},\omega\right)\right] &= C\left(\boldsymbol{x}_{r_i},\boldsymbol{x}_{r_j},\omega\right)\\ &=\sum_{m=1}^{N_s}\sum_{n=1}^{N_s} G^*(\boldsymbol{x}_{r_i},\boldsymbol{x}_{s_m},\omega)G\left(\boldsymbol{x}_{r_j},\boldsymbol{x}_{s_n},\omega\right)E\left[S^*(\boldsymbol{x}_{s_m},\omega)\,S(\boldsymbol{x}_{s_n},\omega)\right],\end{aligned} \tag{3}$$

which can be approximated by the stack over many time intervals, for instance one-hour windows throughout a day. In equation 3, the term $E\left[S^*(\boldsymbol{x}_{s_m},\omega)\,S(\boldsymbol{x}_{s_n},\omega)\right]$ denotes the expected correlation of sources at position $\boldsymbol{x}_{s_m}$ and $\boldsymbol{x}_{s_n}$. The evaluation of equation 3 is prohibitively expensive, not only due to the double summation, but also because many simulations are required for multiple sources.

To reduce computational costs, we assume that the correlation between different noise sources decays relatively quickly with distance compared to the seismic wavelength and that the contribution from collocated noise sources to the correlation function is dominant. We therefore make the approximation

$$E\left[S^*(\boldsymbol{x}_{s_m},\omega)\,S(\boldsymbol{x}_{s_n},\omega)\right]=I(\boldsymbol{x}_{s_n},\omega)\delta(\boldsymbol{x}_{s_m}-\boldsymbol{x}_{s_n}), \tag{4}$$

where $I(\boldsymbol{x}_{s_n},\omega)$ is the PSD of passive source at $\boldsymbol{x}_{s_n}$. For uncorrelated noise sources, the equation 3 condenses to

$$C\left(\boldsymbol{x}_{r_i},\boldsymbol{x}_{r_j},\omega\right)=\sum_{n=1}^{N_s} G^*(\boldsymbol{x}_{r_i},\boldsymbol{x}_{s_n},\omega)G\left(\boldsymbol{x}_{r_j},\boldsymbol{x}_{s_n},\omega\right)I(\boldsymbol{x}_{s_n},\omega). \tag{5}$$

Compared with equation 3, the double summation reduces to single summation in equation 5, thus facilitating the forward computation of noise correlation functions.

LS-ICCM and SP-ICCM

Equation 5 provides a forward map for the calculation of interstation cross-correlograms that can be compared to the observed cross-correlograms. It can be rewritten into a matrix form as

$$\mathbf{d}=\mathbf{Lm}, \tag{6}$$

where $\mathbf{d}$ is a vector of interstation cross-correlograms, $\mathbf{m}$ is a vector of source PSDs, and $\mathbf{L}$ is the forward operator that maps the source PSDs into interstation cross-correlograms.

The optimal estimation of source PSDs can be achieved by minimizing the objective function

$$J(\mathbf{m})=\frac{1}{2}\|\mathbf{W}_d(\mathbf{Lm}-\mathbf{d}_{obs})\|_p^p+\frac{\lambda}{2}\|\mathbf{W}_m\mathbf{m}\|_q^q, \tag{7}$$

where the first term measures interstation cross-correlogram misfit or data misfit, and the second term imposes model regularization. λ is a trade-off parameter for these two terms. $\mathbf{W}_d$ is a matrix of data weights, which is often a diagonal matrix containing the inverse of the standard deviation of the data. $\mathbf{W}_m$ is a matrix of model weights that we can design in order to enhance our preference regarding the model, for example resolution or smoothness. p and q indicate that different norms can be applied to measure the norm of vectors. The solution of equation 7 can be expressed explicitly as

$$\mathbf{m}=(\mathbf{L}^T\mathbf{W}_d^T\mathbf{W}_d\mathbf{L}+\lambda\mathbf{W}_m^T\mathbf{W}_m)^{-1}\mathbf{L}^T\mathbf{W}_d^T\mathbf{W}_d\mathbf{d}. \tag{8}$$

When $p=q=2$ and $\mathbf{W}_m$ is an identity matrix $\mathbf{I}$, the solution of equation 7 is a damped least-squares solution; the inverse of the matrix in parentheses can be solved accurately by matrix decomposition methods or approximately by iterative methods. This damped least-squares solution is similar to the cross-correlation imaging method. Here we refer to the damped least-squares solution as LS-ICCM.

A sparse model can be obtained by simply choosing a norm that does not penalize large elements contained by the model. One common approach is to choose an L_1 norm for the model and an L_2 norm for the data misfit in equation 10. The mixed norm problem can be easily transformed to an L_2-L_2 problem by using a model dependent model weight matrix with elements proportional to

$$[\mathbf{W}_m]_{ii}=\frac{1}{\sqrt{m_i}}. \tag{9}$$

To avoid division by zero, a minimum threshold has to be chosen for $\mathbf{W}_m$. This threshold is set to be percentage of the maximum value in the model vector. The smaller the percentage, the sparser the solution. Hence, this number defines the second trade-off between sparseness and smoothness. The same order of percentage can be used for all frequencies. The actual values will be different, but all of them represent the same relative size of the model.

10.1190/segam2020-3427411.1

Since $\mathbf{W}_m$ depends on the model, it is a nonlinear inverse problem. To invert the matrix in parentheses in equation 14, one of the most frequently used methods is the iteratively re-weighted least-squares (IRLS) algorithm (Scales et al, 1988) because of its simplicity and efficiency. In the IRLS method, the nonlinear inverse problem is solved iteratively by fixing the model weights to certain previous estimation and then invert the matrix in parentheses within each iteration. The model weights are updated at every iteration using the solution of previous linear problem. Here we refer to this sparsity-promoting solution as SP-ICCM.

Examples

In this section, we use synthetic and field data to demonstrate the resolution improvement of SP-ICCM method over ICCM and LS-ICCM methods.

Synthetic data tests

Here 2D acoustic finite-difference modeling method is used to generate synthetic data. We use a part of the Marmousi II model to introduce some complexity into the numerical experiments (Figure 1a). The part of the model we use is $11.2-13.4$ km in the horizontal axis and $5.1-7.7$ km in the vertical axis of the P-wave velocities of the Marmousi II model. Three seismic sources are evenly distributed from x=1.8 km to x=2.2 km with a spacing of 258 m, as denoted by yellow crosses in Figure 1a. These sources from left to right act at the time 0.05 s, 0.1 s and 0.2 s, respectively. Their source functions are Ricker wavelets with the same amplitude and frequency range. 20 receivers with spatial interval of 200 m are placed at the surface to record seismic waves. Since the average velocity above the sources is approximately 5 km/s and the peak frequency of the wavelet is 20 Hz, the estimated wavelength is about 250 m which is similar to the source spacing. Figure 1b shows the acoustic finite-difference modeling data. To make the multi-source test more realistic, strong random noise is added to the synthetic data, as shown in Figure 1c. The SNR of the noisy data is -2.89 dB. Here, SNR is defined as $10\log_{10} E_{signal}/E_{noise}$, where E_{signal} and E_{noise} are the stacking power of signal and noise, respectively.

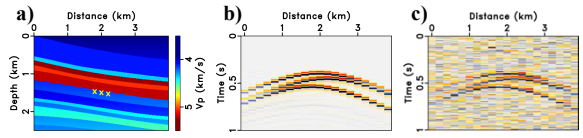

Figure 1: (a) Velocity model. The yellow crosses on the velocity model indicate the true locations of the multi-sources. The receivers are deployed on the surface. Synthetic data (b) without noise and (c) with -2.89 dB noise.

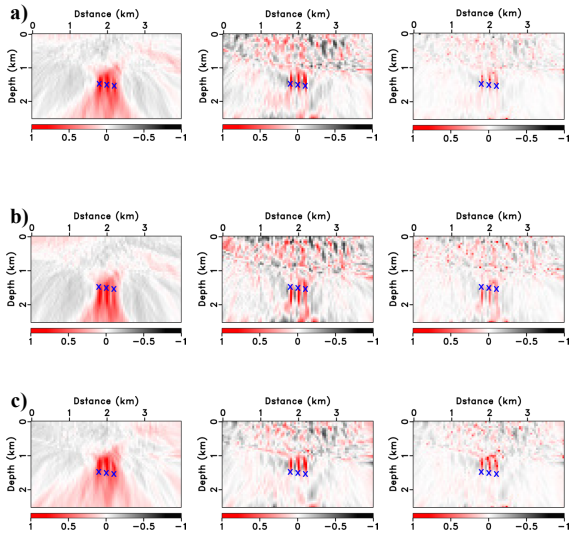

Figure 2: Multi-source images produced by ICCM, LS-ICCM, and SP-ICCM methods using (a) correct velocity, (b) 10% slower velocity, and (c) 10% faster velocity. The left, middle and right columns show the ICCM, LS-ICCM and SP-ICCM images, respectively. The blue crosses indicate the true source locations.

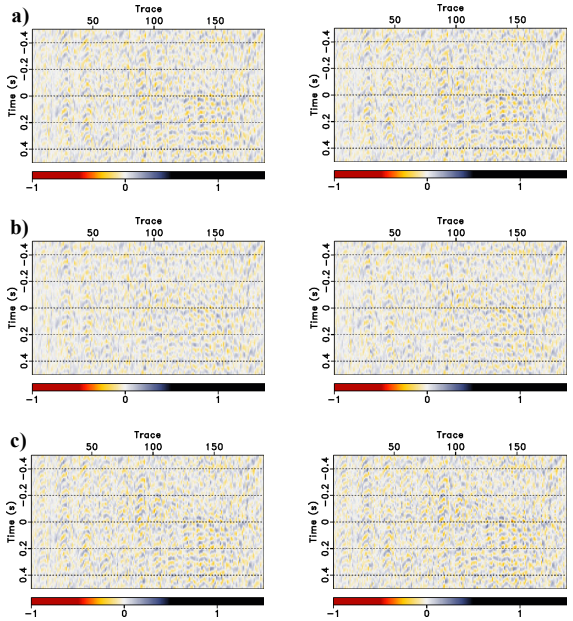

Figure 3: Data residuals of the LS-ICCM and SP-ICCM methods using (a) correct velocity, (b) 10% slower velocity, and (c) 10% faster velocity. The left and right columns show the LS-ICCM and SP-ICCM data residuals, respectively.

We first generate cross-correlograms from observed data by interstation cross-correlation, then invert the source PSDs by

DOI:10.1190/segam2020-3427411.1

minimizing the misfit between the synthetic and observed cross-correlograms. Figure 2 shows the source images produced by the ICCM, LS-ICCM and SP-ICCM methods with correct, 10% slower and 10% faster velocities. From these results, we can see that all these three methods successfully detect multiple source simultaneously even in the presence of strong noises. Compared with the ICCM and LS-ICCM images, the SP-ICCM image also has the highest spatial resolution and SRN. We further calculate the cross-correlogram residuals of LS-ICCM and SP-ICCM methods, as shown in Figure 3. Both LS-ICCM and SP-ICCM methods provide ignorable residuals regardless the velocity is correct or not.

Field data tests

In this part, we demonstrate the effectiveness of the LS-ICCM and SP-ICCM methods with field data recorded on 2D geophone array, which is a part of the 3D acquisition geometry specially designed for seismic while drilling (SWD) trial test in the Middle East. In this SWD test, seismic signals generated by the drill-bit are recorded passively by the seismic sensors on the surface while drilling. One purpose of this test is to locate the relative position of the drill-bit on the subsurface seismic image produced by depth migration of seismic data from surface seismic survey, then the subsurface seismic image can be used for drilling navigation in real time.

Figure 4a shows the 1D velocity model used for source imaging. The model is estimated from a VSP survey. Figure 4b shows the pre-processed shot gather, which is generated from one-hour-long continuous recordings. The pre-processing steps involve producing pilot trace with time-delay correlation, deconvolving the geophone data with the pilot trace and 3D-to-2D conversion by multiplying the data spectra by $\sqrt{i/\omega}$ and then gaining in the time domain by $\sqrt{t}$. In this survey, the offset ranges from -1.6 km to 1.6 km and the receiver spacing interval is 25 m. The minimum offset is 75 m due to the near offsets are not accessible in the field acquisition. The direct wave is very weak as denoted by the red arrows in Figure 4b. Since only the direct wave is needed to estimate the source location, we extract it from the pre-processed data by a 0.1 s window. Additionally, a slope-based filter is applied to the windowed data to improve the event continuity. The extracted direct wave is shown in figure 4c.

Then, we use the pre-processed data to generate cross-correlograms and locate the drill-bit. Figure 5 shows the source images computed by ICCM, LS-ICCM and SP-ICCM methods. Compared these three images, the SP-ICCM migration produces source image with the most accurate location of the drill-bit. Specifically, the SP-ICCM image has the highest spatial resolution and is contaminated by the noise to the least extent. We further compute the data residuals of LS-ICCM and SP-ICCM methods. Both LS-ICCM and SP-ICCM residuals of coherent events are relatively small compared with the input cross-correlograms, as indicated by the red arrows in Figure 6.

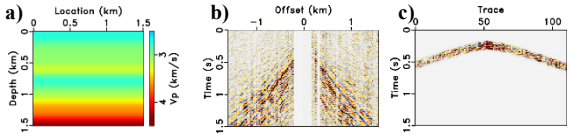

Figure 4: (a) Velocity model. (b) Pre-processed data. (c) Extracted direct wavefield.

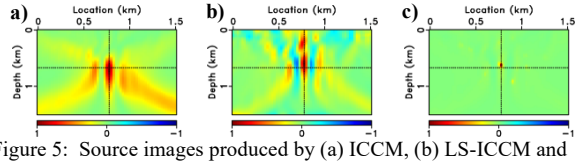

Figure 5: Source images produced by (a) ICCM, (b) LS-ICCM and (c) SP-ICCM methods. The intersection of the black dot lines indicates the true source location.

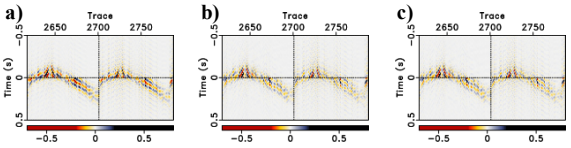

Figure 6: Figure 12. Cross-correlogram comparison. (a) Input cross-correlograms. (b) Cross-correlogram residuals of LS-ICCM method. (c) Cross-correlogram residuals of SP-ICCM method.

Conclusions

We propose a sparsity-promoting cross-correlation waveform inversion method for high-resolution source imaging. This method imposes sparse constraint on the source PSD in space and invert the source PSD by minimizing the observed and simulated interstation cross-correlograms. Compared with conventional ICCM and LS-ICCM methods, the proposed SP-ICCM method generates source image with much higher resolution and is much more robust to the noises in the data. The increase in the spatial resolution of images in SP-ICCM provides a greater ability to separate multiple sources excited close to each other in space and time. Similar to other seismic imaging techniques, SP-ICCM is scale independent, thus it can be applied to source localization from microseismic to crustal scales.

Acknowledgments

Thank Yike Liu from Institute of Geology and Geophysics, Chinese Academy of Science for insightful discussions.

REFERENCES

Aki, K. and P. G. Richards, 2002. Quantitative Seismology, University Science Books.

Basini, P., T. Nissen-Meyer, L. Boschi, E. Casarotti, J. Verbeke, O. Schenk, and D. Giardini, 2013, The influence of nonuniform ambient noise on crustal tomography in Europe: Geochemistry, Geophysics, Geosystems, **14**, no. 5, 1471–1492, doi: https://doi.org/10.1002/ggge.20081.

Ermert, L., A. Villaseñor, and A. Fichtner, 2016, Cross-correlation imaging of ambient noise sources: Geophysical Journal International, **204**, no. 1, 347–364, doi: https://doi.org/10.1093/gjihttps://doi.org//ggv460.

Fichtner, A., 2014, Source and processing effects on noise correlations: Geophysical Journal International, **197**, 1527–1531, doi: https://doi.org/10.1093/gjihttps://doi.org//ggu093.

Hanasoge, S. M., 2013, The influence of noise sources on cross-correlation amplitudes: Geophysical Journal International, **192**, no. 1, 295–309, doi: https://doi.org/10.1093/gjihttps://doi.org//ggs015.

Hanasoge, S. M., 2014, Measurements and kernels for source-structure inversions in noise tomography: Geophysical Journal International, **196**, no. 2, 971–985, doi: https://doi.org/10.1093/gjihttps://doi.org//ggt411.

Maxwell, S. C., J. Rutledge, R. Jones, and M. Fehler, 2010, Petroleum reservoir characterization using downhole microseismic monitoring: Geophysics, **75**, no. 5, 75A129–75A137, doi: https://doi.org/10.1190/1.3477966.

Pujol, J., 2004, Earthquake location tutorial: graphical approach and approximate epicentral location techniques: Seismological Research Letters, **75**, no. 1, 63–74, doi: https://doi.org/10.1785/gssrl.75.1.63.

Scales, J., A. Gersztenkorn, and S. Treitel, 1988, Fast l_p solution of large, sparse, linear systems: Application to seismic travel time tomography: Journal of Computational Physics, **75**, 314–333, doi: https://doi.org/10.1016/0021-9991(88)90115-5.

Schuster, G.T., J. Yu, J. Sheng, and J. Rickett, 2004, Interferometric/daylight seismic imaging: Geophysical Journal International, **157**, no. 2, 838–852, doi: https://doi.org/10.1111/j.1365-246X.2004.02251.x.

Shapiro, S., 2015, Fluid-induced micro seismicity: Cambridge University Press.

Thurber, C. H., and E. R. Engdahl, 2000, Advances in global seismic event location. In Advances in seismic event location: Springer, 3–22.

Waldhauser, F. and W. L. Ellsworth, 2000, A double-difference earthquake location algorithm: Method and application to the northern Hayward fault, California: Bulletin of the Seismological Society of America, **90**, 1353–1368, doi: https://doi.org/10.1785/0120000006.

Zhang, H., and C. H. Thurber, 2003, Double-difference tomography: The method and its application to the Hayward Fault, California: Bulletin of the Seismological Society of America, **93**, 1875–1889, doi: https://doi.org/10.1785/0120020190.